

THE MECHANISM OF ELECTRON ACCELERATION IN TRANS-RELATIVISTIC MAGNETIC RECONNECTION

DAVID BALL,^{1,3} LORENZO SIRONI,² AND FERYAL ÖZEL¹

Draft version December 11, 2018

ABSTRACT

We investigate electron acceleration mechanisms in a low- β electron-proton plasma with moderate magnetization. By varying the guide field and whether or not we trigger reconnection, we vary the number of x-points and plasmoids that form in a given simulation, which we show plays an important role in particle acceleration. Specifically, we show that x-points, either in the primary current layer or in between merging plasmoids are a necessary first step to accelerate electrons out of the cold initial distribution to highly relativistic ($\gamma > 300$) energies. Once an electron goes through this step, it can be further accelerated by different mechanisms that may be energetically dominant compared to the initial acceleration at an x-point, but the vast majority of the highly relativistic ($\gamma > 1000$) electrons across our set of simulations are first accelerated at an x-point. As a result of this, the simulations with more x-points and plasmoids have harder electron spectra than the cases with fewer structures.

Keywords: magnetic reconnection — accretion, accretion disks — galaxies: jets — X-rays: binaries — radiation mechanisms: nonthermal — acceleration of particles

1. INTRODUCTION

Magnetic reconnection is thought to play an important role in accelerating electrons and powering high-energy emission in numerous astrophysical systems including blazar jets (citations), pulsar wind nebulae (citations), gamma ray bursts (citations), the Sun (citations), and accretion flows around black holes (citations). Despite its ubiquity, the physics of particle acceleration through reconnection is not fully understood.

Numerous studies have investigated electron acceleration mechanisms in both relativistic (Nalewajko et al. 2015; Guo et al. 2015; Werner & Uzdensky 2017) and nonrelativistic reconnection (Dahlin et al. 2014; Li et al. 2017; Wang et al. 2016). These studies generally take one of two approaches: some apply a guiding center formalism (e.g., Dahlin et al. 2014) in which they can cleanly separate different acceleration mechanisms in the energy equation for a single particle and ultimately assess the various contributions solely by looking at cell averaged currents, velocities, and fields. However, this formalism breaks down at x-points in anti-parallel reconnection, where the magnetic field vanishes. Others look at individual particle trajectories to assess where and by what mechanisms particles are being accelerated. However, these studies have so far sparsely sampled a collection of representative particles. Furthermore, most of these studies employ either a pair-plasma or a significantly reduced mass ratio.

These previous studies have highlighted a few distinct acceleration mechanisms. One such mechanism is acceleration by the out-of-plane (i.e., in the direction of $\vec{\nabla} \times \vec{B}$) electric field at x-points (citations). These x-points can occur not only in the initial current sheet via the primary or secondary tearing mode, but also in the cur-

rent sheets generated between merging plasmoids, where reconnection also occurs. Another prominent mechanism is Fermi reflection, enabled by the various macro-scale motions induced by reconnection. Fermi reflection can occur between merging plasmoids (citations), within contracting plasmoids (citations), and also between outflows and plasmoids (citations). Nalewajko et al. (2015) also found that particles are accelerated in the trailing edges of plasmoids as they move.

In Ball et al. (2018) we investigated particle acceleration in the trans-relativistic regime and found preliminary evidence for the role of x-points, plasmoids, and Fermi-type processes by examining the histories of a few representative high-energy particles. We did not, however, examine a statistically meaningful sample of particles. In that study, we observed that at low- β , electron acceleration is characterized by extremely short periods of intense acceleration by a non-ideal electric field at x-points in the initial sheet or between merging plasmoids. In contrast, at high- β when electrons start out relativistic, x-point acceleration is negligible, and Fermi reflection dominates. The reason for this is twofold; first, the secondary tearing mode is suppressed at high- β ; second, the energy gain via Fermi reflection off of features moving at the Alfvén speed dominates over the energy gain at x-points.

In this paper, we investigate the physical mechanisms of electron acceleration by comparing four simulations in which we vary the number of x-points and plasmoids by changing guide field strength and whether or not we trigger reconnection. We address the issues of downsampling in time and particle number, as well as the reduced mass ratio by performing simulations with the realistic electron-proton mass ratio while including particle acceleration diagnostics that are calculated on-the-fly during the simulation for all of the particles. We also employ robust methods of identifying x-points and track the role of the work done parallel to the local magnetic field in order to investigate the detailed histories of the accelerated

¹ Department of Astronomy and Steward Observatory, Univ. of Arizona, 933 N. Cherry Avenue, Tucson, AZ 85721, USA

² Department of Astronomy, Columbia University, 550 West 120th Street, New York, NY 10027, USA

³ Email: davidrball@email.arizona.edu

particles.

We find that x-points and plasmoid mergers play critical roles in accelerating electrons in the trans-relativistic regime. In particular, we find that when the secondary tearing mode is active, electron acceleration is significantly enhanced and occurs throughout the domain. In these cases, x-points and plasmoid mergers are ubiquitous and play comparable roles in accelerating electrons. In contrast, when the secondary tearing mode is suppressed, high-energy acceleration is localized to the primary x-point(s) and the mergers of primary plasmoids, which are very few relative to the copious secondary x-points and plasmoids that occur when secondary tearing is active.

2. METHODS

2.1. *Simulation Setup*

We perform four fiducial simulations of magnetic reconnection using the publicly-available code TRISTAN-MP (Buneman 1993; Spitkovsky 2005). We employ a two-dimensional (2D) simulation domain in the xy plane, but we track all three components of velocity and electromagnetic field vectors. We set up the system in Harris equilibrium, with a magnetic field profile $\mathbf{B} = -B_0 \tanh(2\pi y/\Delta) \hat{x}$, where B_0 is the strength of the reconnecting field in the ambient plasma and Δ is the thickness of the sheet. B_0 is related to the magnetization parameter σ via $\sigma = B_0^2/4\pi w_0$, where w_0 is the enthalpy density of the ambient plasma $w_0 = (\rho_e + \rho_i)c^2 + \hat{\gamma}_e u_e + \hat{\gamma}_i u_i$, with $\rho_{i,e}$, $\hat{\gamma}_{i,e}$, and $u_{i,e}$ being the mass densities, adiabatic indices, and internal energy densities of ambient protons and electrons, respectively. We include an out-of-plane magnetic field (referred to as a guide field) and specify its strength as a fraction of the reconnection component, B_g/B_0 . We specify the temperature through the proton β , defined as $\beta \equiv \beta_i = 8\pi n_i k T_i / B_0^2$, where $n_i = \rho_i/m_i$ is the proton number density, T_i is the proton temperature, and m_i is the proton mass. Ambient electrons and protons start with the same temperature, so $\beta_e = \beta_i = \beta$ (the total plasma beta, including both species, is 2β). In our low- β case of $\beta_i = 0.003$, the ambient protons are non-relativistic, so the magnetization parameter as defined with the proton rest mass $\sigma_i = B_0^2/4\pi\rho_i c^2$ is nearly identical to the enthalpy-weighted magnetization σ defined above. Each computational cell in the ambient plasma is initialized with four particles per cell ($N_{ppc} = 4$).

2.2. *Parameter Scans*

Our goal in investigating the acceleration mechanism is to create density and field structures that are drastically varied and examine how this affects particle acceleration. We find that one numerical and one physical parameter can control the structure of the current sheet and give us a great diversity of current layers just by changing the simulation setup and guide field strength. Specifically, for our particular values of σ and β , when we include a guide field of strength $B_g/B_0 = 0.3$, it effectively suppresses the formation of x-points and plasmoids. Additionally, by triggering reconnection or allowing it to evolve spontaneously, we can alter the number of x-points and plasmoid mergers.

We show snapshots from our four simulations in Figure 1. Here, the top row shows snapshots of density from

the simulations with $B_g/B_0 = 0.1$ while the bottom row shows snapshots from simulations with $B_g/B_0 = 0.3$. The left column shows the triggered simulations while the right column shows the untriggered simulations. We see that, for the particular σ and β we use here, a guide field with strength $B_g/B_0 = 0.3$ increases the width of the current layer and results in thicker, more stable current sheets that do not fracture via the secondary tearing mode. This is in stark contrast with lower guide field simulations at the same σ and β (top row), where the current sheet fractures copiously into x-points and plasmoids.

All PIC studies of reconnection have to make the choice of whether to trigger reconnection at specific point in the current sheet or to let it evolve spontaneously, but the implications of this choice are not fully understood. In a triggered setup there is one primary x-point and the Alfvén crossing time is greater than the primary tearing timescale. Because of this, a single large magnetic island forms at the boundary when the reconnection fronts collide, and no other primary plasmoids form. Instead, in the region vacated by the reconnection fronts, the secondary tearing mode (when active) forms x-points and plasmoids in the center of the domain which are pulled to the edges of the box and ultimately merge with the large boundary island. In contrast, in an untriggered setup, numerous primary x-points and plasmoids form via the primary tearing mode. These primary plasmoids then hierarchically merge until there is one large magnetic island. In this way, the untriggered setup invariably has more primary x-points as well as more large plasmoid mergers than a triggered setup with the same physical parameters. One can make arguments for the applicability of either choice to realistic situations. However, here we utilize both as a numerical tool to achieve a diversity of density and electromagnetic field structures to enable us to track electron acceleration under these varied conditions.

3. DIAGNOSTICS OF ACCELERATION

In this section, we describe how we explore the acceleration mechanisms through a combination of tracking particle acceleration histories as well as identifying x-points from the structure of the electromagnetic fields. In subsection 3.1, we describe the properties of particles that we track that inform our understanding of their acceleration history. In 3.2, we describe our method for identifying x-points from the structure of the magnetic field. Finally, in 3.3, we define the criterion we employ to associate acceleration episodes with either x-points or mergers.

3.1. *Tracking Particle Properties*

In Ball et al. (2018), we found that electrons generally experience extremely short episodes of acceleration, characterized by sudden jumps in their energy, rather than a steady and continuous energy gain. This presents a problem in accurately identifying the time and location of particle acceleration episodes because the output cadence is often drastically down-sampled in time from the actual simulation timesteps. In other words, by the time the simulation produces an output file, the particle may have moved significantly from where it was accelerated, and we lose the ability to accurately identify where and when the particle was accelerated. In addition, particle

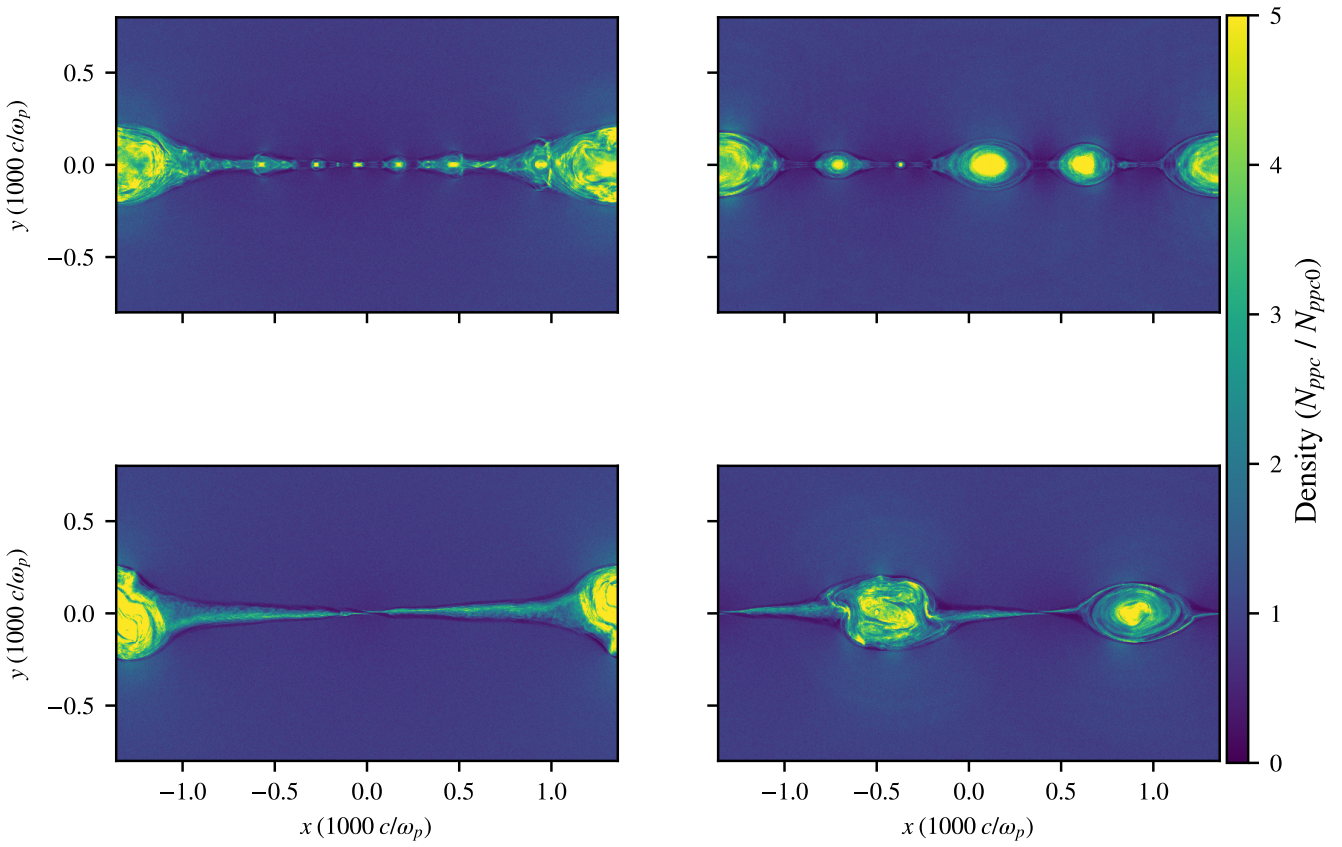


Figure 1. Snapshots of density from our four fiducial simulations. The left column shows the simulations with zero guide field and the right column shows the simulations with a guide field. The first row shows simulations where reconnection is triggered by hand, and the second row shows simulations where reconnection develops spontaneously, resulting in more plasmoids than their triggered counterparts.

outputs are also typically down-sampled in number due to the large number of particles necessary for PIC simulations. Typically only a small fraction of particles are saved in the output files for analyzing.

In order to get around these problems, we track four additional properties of the particles on-the-fly during the simulation. These properties are the time and location of the particle when its Lorentz factor γ first exceeds $\sigma_e/2$, the magnitude and direction of E_z , the z-component of the electric field at this time, and also the cumulative work done on particles by the z-component of any electric field that is parallel to the local magnetic field. We will discuss our reasons for saving these particular quantities in section ???. These quantities are useful diagnostics for understanding the acceleration mechanisms: the time and location of the particle's acceleration allow us to explore what structures in the simulation the particle is interacting with during the time of its acceleration. The sign of E_z at this time helps us distinguish between acceleration at x-points in the primary current layer versus x-points at the interface of merging plasmoids. Finally, the work done by the z-component of parallel electric fields is

$$W_{||,z} = \int_{t_0}^t qE_{||,z}v_z dt \quad (1)$$

where $E_{||} \equiv \vec{E} \cdot \hat{b}$, and $E_{||,z}$ is the z-component of $\vec{E}_{||}$, so $E_{||,z} \equiv E_{||}\hat{b} \cdot \hat{z}$. This quantity is useful because it allows us to isolate work done by non-ideal electric fields associated with magnetic fields in the $x-y$ plane reconnecting other mechanisms that accelerate particles in the $x-y$ plane such as Fermi-type acceleration in regions of high velocity convergence.

By checking for the $\gamma > \sigma_e$ condition at every simulation timestep and recording the time and position when this criterion is satisfied, we overcome the time-downsampling problem mentioned previously. Additionally, we track and analyze these properties for all of our particles, not just a downsampled selection. We note, however, that this method will only capture the first acceleration episode that a particle experiences. This first episode, however, is critical to promoting the electron to relativistic energies, where it can then sample large-scale velocity differences and become further energized through Fermi-type processes. In order to explore acceleration after the particle's promotion out of the cold $\gamma \approx 1$ population to highly relativistic velocities, we also follow a sample of particle trajectories and explore the contributions of $E_{||,z}$ to the energization of a typical high-energy particle. In general, we find that particles are almost always first accelerated by $E_{||,z}$ at an x-point, and then are further accelerated by a combination of $E_{||}$ in current sheets during plasmoid mergers and E_{\perp} in the interaction of outflows with plasmoids and the dissipation of turbulent motions within plasmoids.

3.2. X-point Identification

In order to test the association of electron energization episodes with x-points, we first identify x-points from the cell averaged fields. Haggerty et al. (2017) recently studied the statistics of x-points in turbulence via PIC simulations and explored methods to robustly identify

x-points. In a 2.5D setup such as ours, x-points correspond to saddle points in the z-component of the magnetic vector potential, A_z . Following Haggerty et al. (2017), we first apply a Gaussian filter with a width of $\sim 4 c/\omega_p$ to the z-component of the magnetic vector potential, A_z . We then identify critical points where $\partial A_z/\partial x = \partial A_z/\partial y = 0$. In order to distinguish between local minima, maxima, and saddle points, we calculate the matrix of second derivatives (or, Hessian matrix),

$$H_{ij} = \frac{\partial^2 A_z}{\partial x_i \partial x_j}.$$

If the eigenvalues of this matrix are negative, this corresponds to a maximum in A_z , if both are positive, it corresponds to a minimum. If, however, the eigenvalues are of opposite sign, then this is a saddle point and we identify it as an x-point. We show in Figure 2 a snapshot from our untriggered simulation with a guide field, where a large plasmoid merger occurs at the end of the simulation. We plot the locations of x-points identified with the method described above with red x's. We see that we are able to identify x-points not only the initial horizontal current sheet, but also x-points generated in the current sheets at the interface of merging plasmoids.

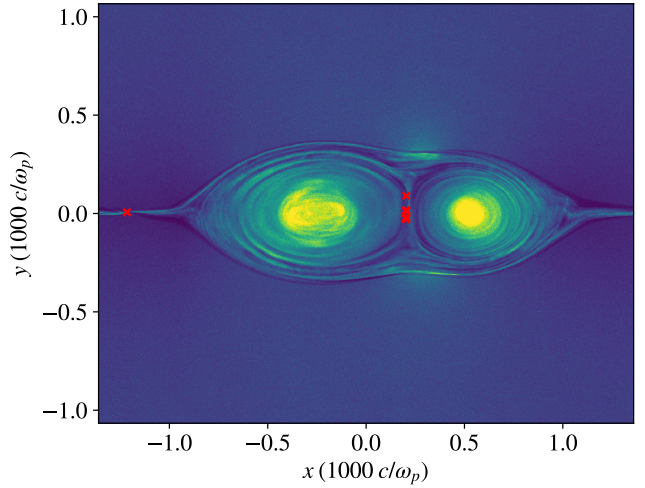


Figure 2. Snapshot of density from an untriggered simulation showing a large plasmoid merger as well as an x-point in the horizontal current sheet. We show with red X's where the x-point identification algorithm picks out x-points at this snapshot. We see we are able to successfully identify x-points in both the horizontal and vertical current sheets.

3.3. Distinguishing Criteria for Acceleration Mechanisms

We use a few simple criteria to distinguish between particles that are accelerated near an x-point in the initial horizontal current layer from those at the interface of two merging plasmoids. If a particle is accelerated at an x-point in the initial horizontal current layer, then we expect the particle to be suddenly accelerated by a non-ideal out-of-plane electric field in the direction of $\vec{\nabla} \times \vec{B}_0$ when it enters the current layer at an x-point. Reconnection also occurs in vertical current sheets formed between merging plasmoids where particles may also be accelerated. A particle that is accelerated in a merging event

will likely first interact with the current sheet by entering a plasmoid. During this process, the particle will be heated due to the compression while the plasmoid forms. The plasmoid will then merge with another plasmoid in the current layer, developing a vertical current sheet between them. The sign of the electric field in these vertical current layers associated with mergers, however, is in the opposite direction from x-points in the initial layer (i.e., in the direction of $-\vec{\nabla} \times \vec{B}_0$).

We illustrate this in Figure 3, where we show in-plane magnetic field lines superimposed on a snapshot of density from the triggered simulation with a guide field. We see a typical x-point in the horizontal current layer, highlighted by a cyan box. Note that $\vec{\nabla} \times \vec{B}$ in this region is in the $+\hat{z}$ direction. At $x \approx 0.6$ we see a secondary plasmoid merging into the large boundary island. A vertical current sheet forms and reconnection proceeds, with $\vec{\nabla} \times \vec{B}$ in the $-\hat{z}$ direction.

To find all the particles at a given time that are accelerated by x-points, we first identify x-points from the fields as described above in 3.2. Generally, after a particle is accelerated at an x-point, it either enters a plasmoid or an outflow and moves away from the x-point. The outflow moves at $\sim v_A$, while plasmoids generally move slower than this; the maximum speed that particles move away from x-points is $\sim v_A$. Because of that, we look for all particles that have acceleration episodes that are Alfvénically connected to an x-point, i.e., we require that

$$\left| \frac{x_{cs} - x_{xpoint}}{t_{cs} - t_{xpoint}} \right| \leq v_A. \quad (2)$$

In order to identify particles that are associated with mergers, we exploit the geometry of reconnection at the interface of merging plasmoids. As mentioned above, in a plasmoid merger, the sign of the electric field will be opposite that in the horizontal current layer's x-points. As such, if the E_z field is negative at the time of a particle's acceleration, we identify the acceleration episode as being due to a merger.

If neither of the above criteria are met, we classify the episode as “other”. We find that these uncategorized episodes generally produce much lower-energy particles than x-points or mergers, and they are often associated with plasmoid motion, contraction, or the interaction of an outflow with a plasmoid.

We note that with our classification scheme, while all of the particles accelerated at an x-point will be identified correctly, it will also classify particles that were accelerated near the x-point through other mechanisms. In other words, this scheme has high recall but low precision.

4. ACCELERATION RESULTS

In order to assess the relative importance of x-points and plasmoid mergers to the overall electron energy spectra, we iterate through time over all of our simulations and examine the cumulative spectra from the different acceleration mechanisms. That is, at each output timestep, we identify the location of x-points as described in Section 3.2. We then associate all the particles with an acceleration mechanism as described in Section 3.3. We then construct time-integrated energy spectra from

these different components and assess their relative importance.

We show in Figure 4 three snapshots in time from the triggered simulation with a guide field strength of $B_g = 0.3B_0$, where the secondary tearing mode is suppressed. Each timestep is depicted with two panels: the top panel shows the density profile, and the bottom panel depicts the location where the particle first exceeds $\sigma_e/2$ versus the particle's final energy.

We see that at an early time (top two panels), there is a single primary x-point accelerating particles to high energies. As reconnection proceeds, a single secondary plasmoid begins to develop in the middle of the domain (middle two panels), and there are two corresponding secondary x-points on either side. These secondary x-points accelerate particles, but not as prolifically as the initial primary x-point. Eventually, the plasmoid is pulled towards the left edge of the domain (bottom two panels) and merges with the large boundary island. A current sheet forms between the two plasmoids and their magnetic fields reconnect, serving as another site of acceleration, with the expected flip in E_z polarity from the x-points in the initial current sheet.

We show the time-integrated spectra from the different mechanisms in Figure 5. In this case, almost all the highest energy particles ($\gamma > 1000$) come from x-points, and in particular, the primary x-point. This is because the guide field suppresses secondary plasmoid formation, resulting in only one merging event over the course of the simulation. We note that because acceleration is so localized in this case, in the limit of very large domains, the acceleration region will comprise a vanishing fraction of the total domain and we expect acceleration to be negligible.

In order to explore the effect of having numerous primary x-points, we show in Figure 6 snapshots from the untriggered simulation with the same guide field strength of $B_g = 0.3B_0$. At early times (top two panels), we see the primary tearing mode pinch the current sheet at three locations, resulting in three primary x-points, all of which serve as sites of particle acceleration. In the middle two panels, we see two of the primary plasmoids merging at $x \approx 0.77$, accelerating numerous particles. In an untriggered setup, such as this one, the primary plasmoids hierarchically merge, resulting in very large plasmoid mergers at late times, which we see in the bottom panels. As these large plasmoids merge, they accelerate a large number of particles as their magnetic fields reconnect.

We show the cumulative spectra from this simulation in Figure 7. We see that the x-points are still the dominant source of high-energy particles, but now the mergers also generate a larger number of high-energy particles as compared to the previous triggered simulation. This is because mergers are inevitable in an untriggered setup, as long as the dominant wavelength of the tearing mode produces numerous primary x-points (and hence, plasmoids) in the given domain. We note that the contributions to high-energy particle acceleration between x-points and mergers is likely a function of the number of x-points per unit length in the sheet. As such, the initial thickness of the current sheet in an untriggered setup plays an important role in setting the relative importance of x-points and mergers, and will affect the

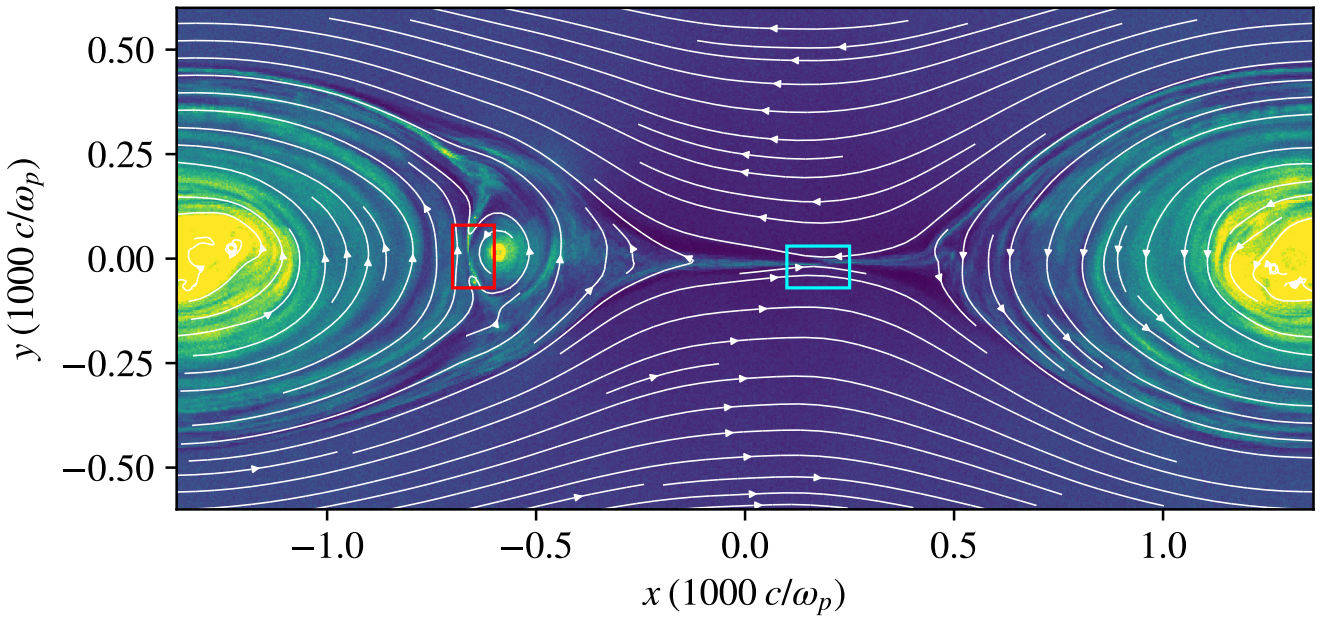


Figure 3. Snapshot of density from a triggered simulation with a guide field. We superimpose streamlines of the in-plane magnetic field and emphasize two regions: the cyan box where reconnection is taking place in the initial horizontal current layer, and the red box, where reconnection is occurring between two merging plasmoids. Note that the sign of $\vec{\nabla} \times \vec{B}$, and hence the sign of the electric field is positive in the horizontal layer (cyan box), and negative in the vertical current layer between plasmoids (red box).

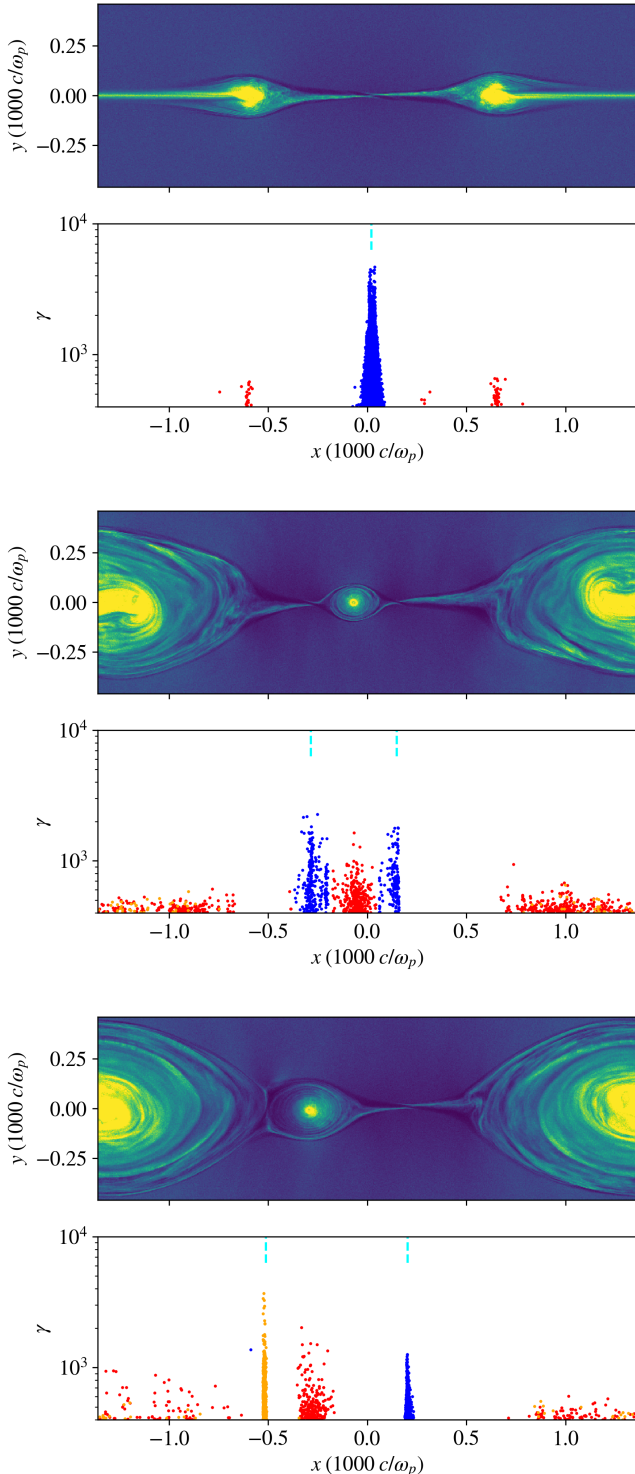


Figure 4. Snapshots at three different times from the triggered simulation with a guide field strength of $B_g = 0.3B_0$. X-points are the dominant sites of electron acceleration and there are very few of them throughout the simulation. One secondary plasmoid forms (middle panel), and eventually merges into the boundary island (bottom panel), which also accelerates some particles.

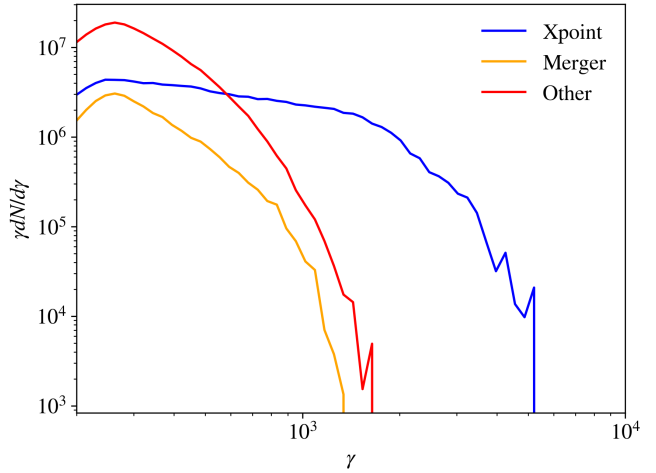


Figure 5. Time-integrated electron spectra from the triggered simulation with guide field decomposed by acceleration mechanism. X-points dominate all of the highest-energy electron acceleration.

overall spectrum of non-thermal particles.

We show in Figure 8 three snapshots from the triggered simulation with no guide field. We see at early times that numerous closely-spaced secondary x-points have already formed in the region vacated by the reconnection fronts. Two small plasmoids at $x \approx 0.1$ are merging. Due to the prevalence of the secondary tearing mode and associated plasmoid mergers, acceleration is not as localized as in the previous cases with a guide field. This trend continues in the middle panel, where secondary x-points are accelerating particles all throughout the central $\sim 1/3$ of the domain. The secondary plasmoids that form are inevitably pulled towards the edge of the domain, ultimately merging with the large boundary island, accelerating particles in merging events. This trend continues to later times (bottom panels): acceleration at secondary x-points and the associated merging of secondary plasmoids remains active until the magnetic island at the boundary grows so large that it chokes off the inflowing plasma and reconnection halts.

When we compare the relative contributions of x-points and mergers to the electron energy spectrum, in Figure 9, we find that both x-points and mergers accelerate a large number of particles above $\gamma = 1000$. Mergers slightly dominate over x-points in overall number of particles that are accelerated to these highly relativistic energies.

We finally explore the case of an untriggered simulation with no guide field. We show in Figure 10 three snapshots from this simulation. At early times (top panel), numerous primary and x-points quickly form and begin accelerating particles all throughout the domain. These primary and secondary plasmoids hierarchically merge until the largest plasmoids in the domain merge (middle panel). Once the largest plasmoid is formed (bottom panel), the secondary tearing mode remains active, producing numerous secondary x-points and plasmoids throughout the domain. We show in Figure 11 the cumulative electron spectra broken down into components. We see again that both x-points and mergers produce large numbers of high-energy electrons, with mergers being slightly more dominant.

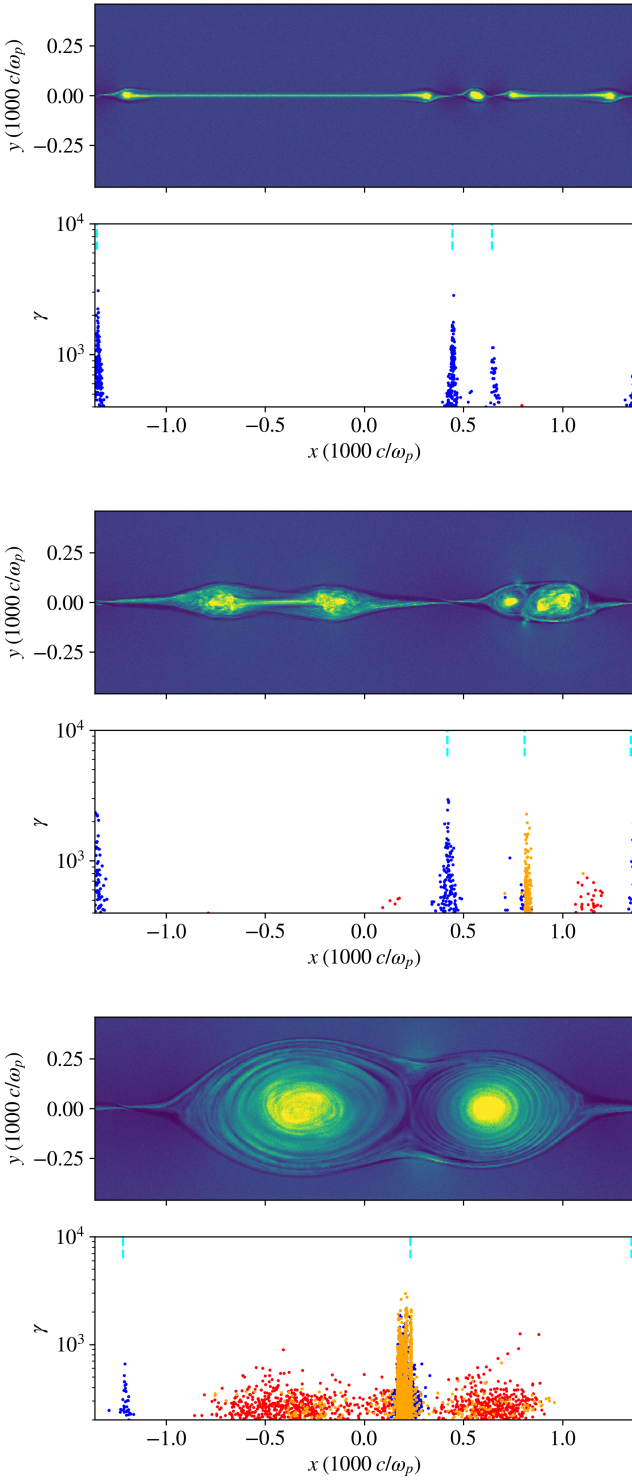


Figure 6. Snapshots at three different times from the untriggered simulation with a guide field strength of $B_g = 0.3B_0$. Because we do not trigger reconnection, numerous primary x-points form and we see numerous primary x-points and plasmoid mergers throughout the simulation domain.

5. TEST PARTICLES

In the previous sections we explored where electrons are first accelerated and found that x-points appear to be important structures in regulating the production of

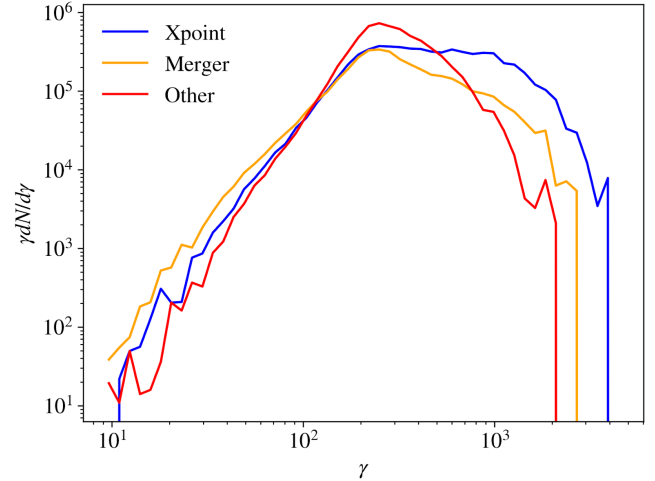


Figure 7. Time-integrated electron spectra from the untriggered simulation with guide field of strength. While x-points still dominate the highest-energy acceleration episodes, mergers play a much more significant role than in the triggered case (Figures 4 and 5).

a non-thermal electron spectrum. In this section, we explore in more detail the energetics and dynamics of electrons that are accelerated by the non-ideal electric fields near an x-point.

As previously discussed, x-points have a strong non-ideal out-of-plane (in the $\pm\hat{z}$ direction) electric field associated with them. This electric field is aligned with the guide field resulting in a large $|\vec{E} \cdot \hat{b}|$ with the dominant component being from the z-aligned electric field near the x-point. We show the structure of $E_{||}$ and its various components from our triggered simulation with $B_g = 0.3B_0$ in Figure 12. We see that the parallel electric field near the x-point is dominated by the z-component of the electric field, as expected. In the outflows, however, there is a significant component of $E_{||}$ in the x-direction (along the outflow). Ultimately we will see that when particles interact with the z-aligned electric field near the x-point, that they are likely to be accelerated beyond the thermal peak of the spectrum into a non-thermal tail, whereas particles that interact with $E_{||}$ along the outflow make up the thermal peak of the distribution.

We show the evolution of an electron's Lorentz factor as well as the work done by the z-component of the parallel electric field from the triggered simulation with $B_g = 0.3B_0$ in Figure 13. This electron's evolution is typical of high-energy particles from this simulation. We see that the particle is suddenly accelerated by a strong $E_{||,z}$ (where $E_{||,z} = \vec{E}_{||} \cdot \hat{z}$) field when it interacts with the x-point. After this, the particle can be further accelerated by other mechanisms (e.g., parallel electric fields in the outflow, dissipation of turbulence in magnetic islands, plasmoid mergers), but the fractional energy gain of the particle is dominated by its interaction with the x-point.

In order to more thoroughly test our finding that non-thermal acceleration is largely controlled by x-points, we include populations of test particles that only feel certain components of $\vec{E}_{||}$. These particles are evolved simultaneously to the normal particles but do not deposit their currents onto the grid. We use two sets of test particles to explore the energization mechanism of electrons. One

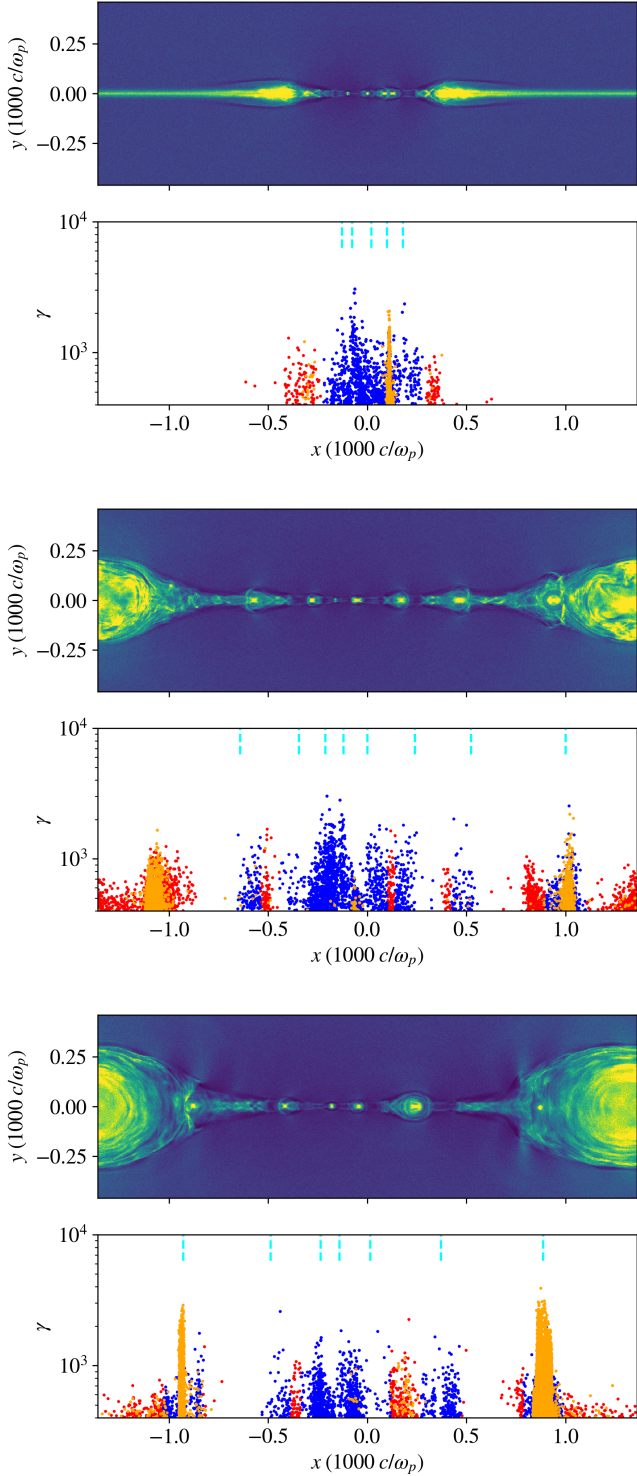


Figure 8. Snapshots at three different times from the untriggered simulation with no guide field. The secondary tearing mode fractures the current sheet throughout the domain, resulting in numerous x-points and secondary plasmoids.

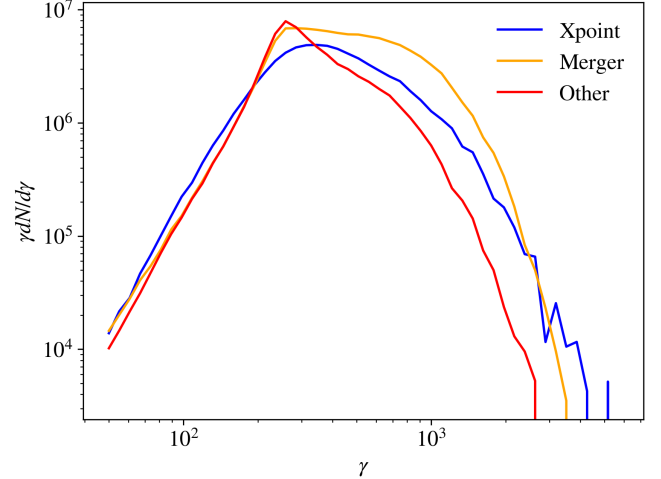


Figure 9. Time-integrated electron spectra from the triggered simulation with no guide field. We see that the copious production of secondary plasmoids leads to mergers dominating over x-points for high-energy acceleration.

set of test particles does not feel any electric fields parallel to magnetic fields (i.e., $W_{||} = 0$), and the other set does not feel any z-component (out-of-plane) of the $E_{||}$ field.

We show the spectra of these different populations of particles in Figure 14 for the triggered simulation with $B_g = 0.3B_g$. We see that the particles that do not experience any $E_{||}$ (red dotted line) are only slightly heated beyond their initial thermal distribution. This demonstrates that both bulk heating and non-thermal acceleration are mediated by parallel electric fields. The particles that don't experience $E_{||,z}$, however, have a thermal peak that is consistent with the normal particles $\gamma \approx 100$, but shows no evidence of a non-thermal distribution above this thermal peak. This confirms our hypothesis that the non-thermal tail of the distribution is controlled by the parallel electric field in the z-direction associated with the x-point. The thermal peak is still able to form because particles that enter the current layer in the outflow primarily interact with the outflow-aligned electric field, $E_{||,x}$.

6. CONCLUSIONS

7. APPENDIX A: SHEET THICKNESS

Explore how the current sheet thickness affects the number of x-points per unit length, and hence energy spectra in an untriggered setup (probably in guide field case, probably in no guide field case, secondary plasmoid formation causes fracturing all over anyways and we have a similar number of x-points per unit length)

8. APPENDIX B: BOX SIZE

Look at case of triggered vs. untriggered as function of boxsize (with guide field), should see a much steeper dependence of triggered case as opposed to untriggered

9. APPENDIX C: ANTI-PARALLEL AND LOW GUIDE FIELD COMPARISON

We show in Figure 15 the spectra from simulations with identical physical parameters except for a changing guide field, with values of $B_g/B_0 = 0, 0.1$ and 0.3 . We see that the spectra from $B_g/B_0 = 0$ and $B_g/B_0 = 0.1$

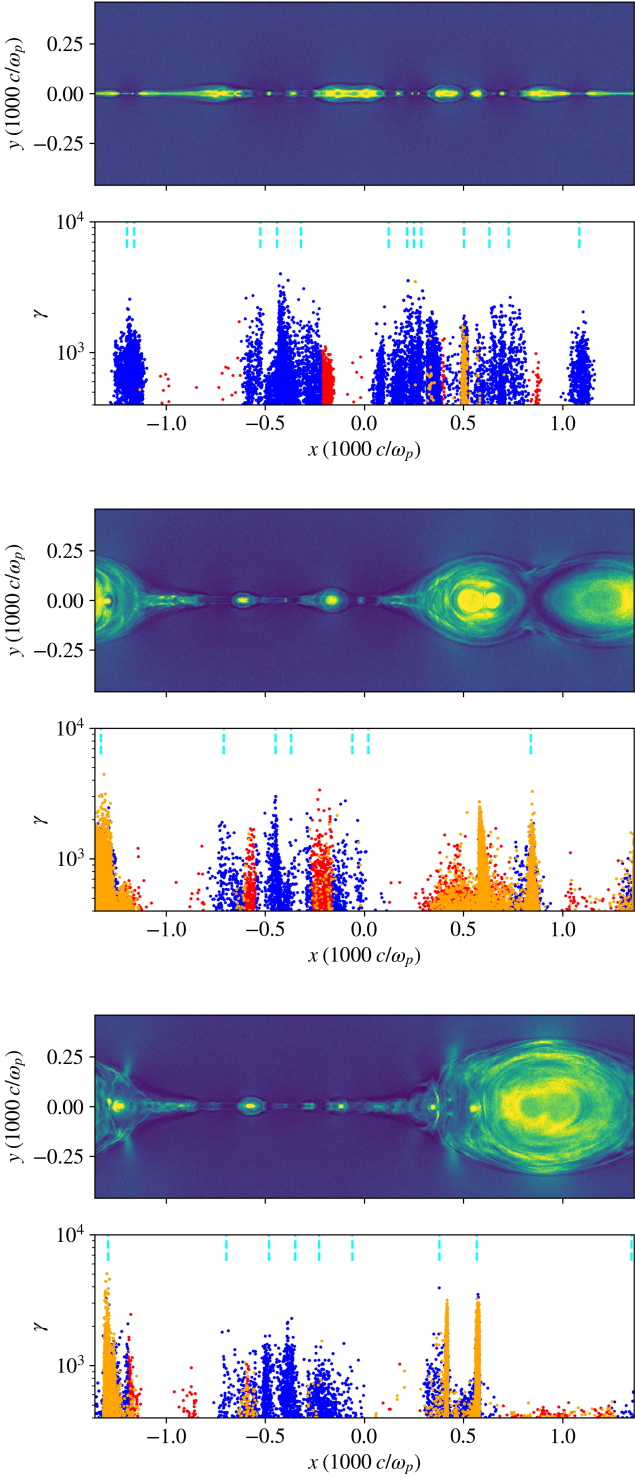


Figure 10. Snapshots at three different times from the untriggered simulation with no guide field. We see that both the primary and secondary tearing mode result in copious x-point and plasmoid formation and the corresponding electron acceleration.

cases are remarkably similar, with nearly identical power-law slopes. We additionally examine the typical structures present in each simulation, shown in Figure 16. We in the two lowest guide field cases that numerous x-point and plasmoids form, which ultimately result in similar

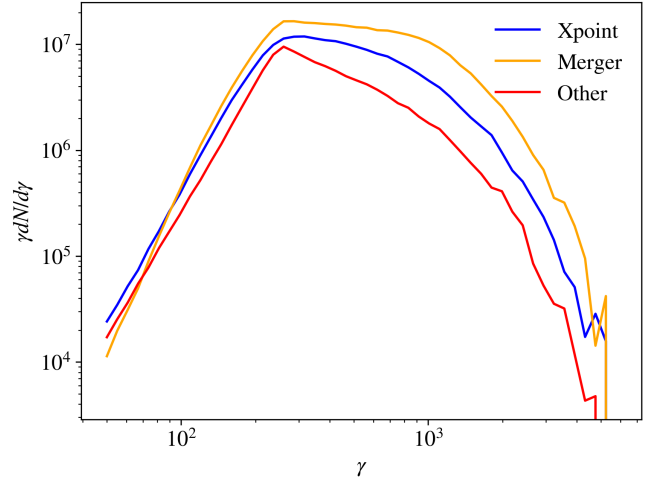


Figure 11. Time-integrated electron spectra from the untriggered simulation with no guide field. The prevalence of plasmoids (both primary and secondary), and their merging results in plasmoid mergers dominating over x-points for high-energy acceleration.

spectra. In the $B_g = 0.3$ case, however, the structure of the current layer changes dramatically, and these differences are reflected in the spectrum.

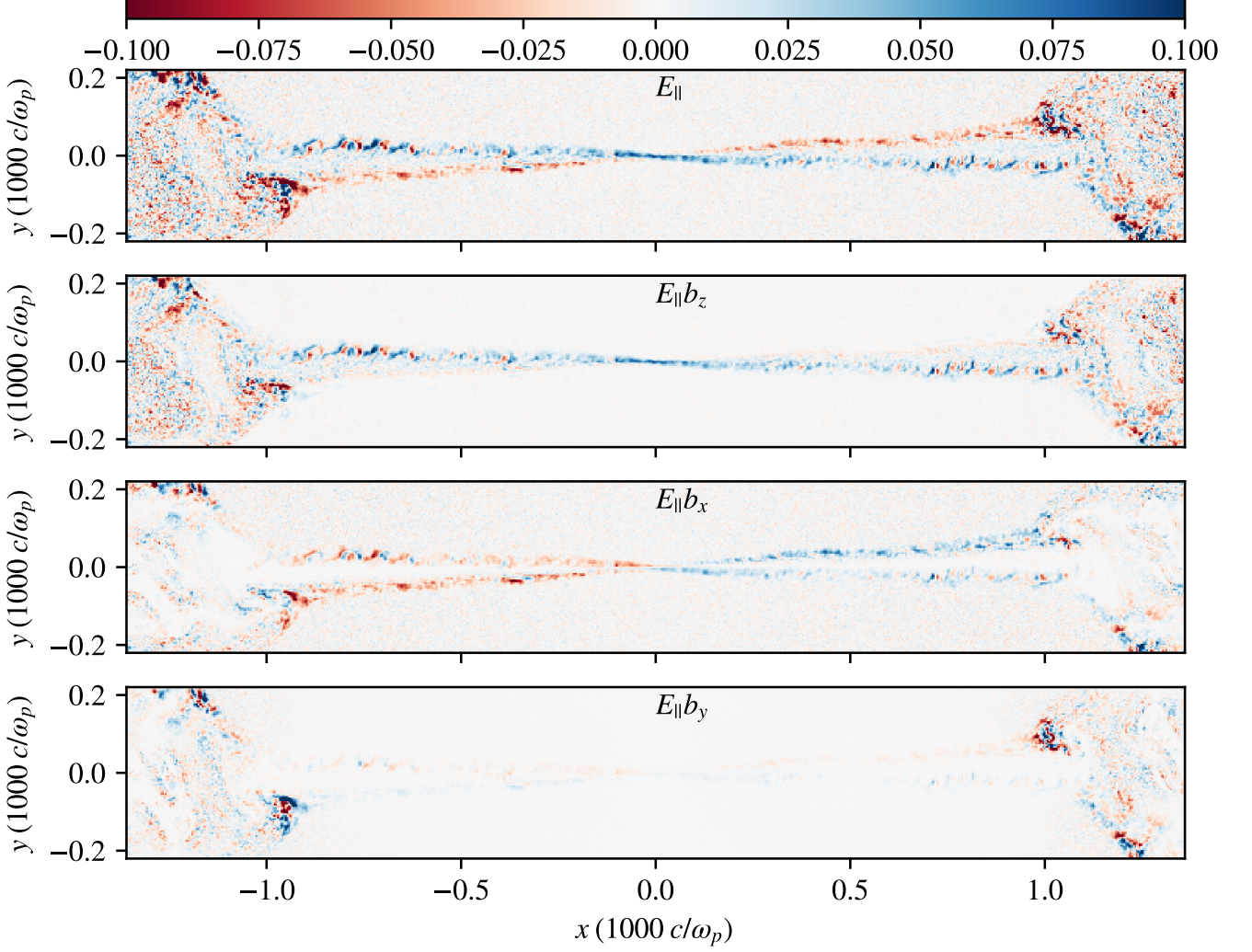


Figure 12. Profiles of the parallel electric field (top), decomposed into its Cartesian components (bottom three) for a high-energy electron from the triggered simulation with $B_g = 0.3B_0$. We see that the parallel electric field near the x-point is dominated by the z-component associated with the dissipation at the x-point. A significant parallel electric field persists in the edges of the outflow, largely from the x-component of $E_{||}$. The y-component is negligible except in small localized regions where the dense parts of the outflow are impacting the magnetic island, generating turbulent motions in the large boundary island (i.e., at $x \approx \pm 1$, $y \approx \pm 1$ in the bottom panel).

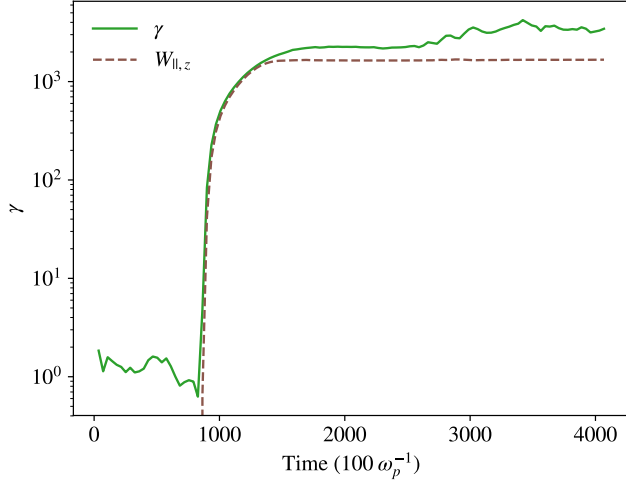


Figure 13. Evolution of Lorentz factor and the z-component of parallel work, $W_{||,z}$, of a typical high-energy electron from the triggered $B_g = 0.3B_0$ simulation. The electron is first accelerated at an x-point by a strong parallel electric field in the z-direction. After this initial acceleration the electron gains energy through other means.

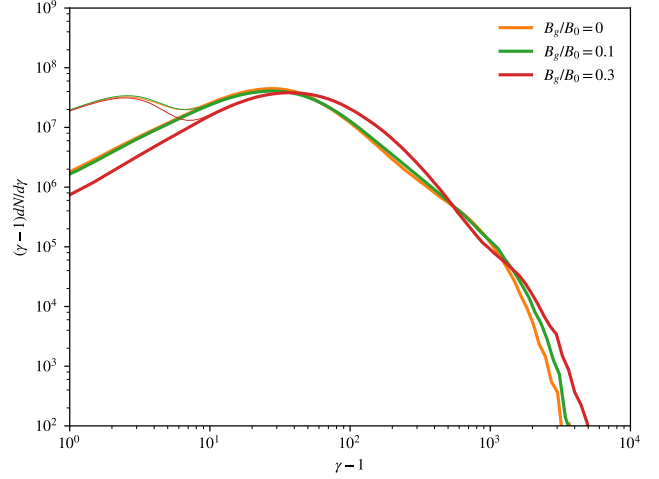


Figure 15. Electron energy spectra for simulations with varying guide field. The zero guide field case is shown in orange and $B_g = 0.1B_0$ and $B_g = 0.3B_0$ are shown with the green and red lines, respectively. We see that the zero guide field and low guide field spectra are nearly identical, while the higher guide field case shows more overall heating, but a steeper spectrum.

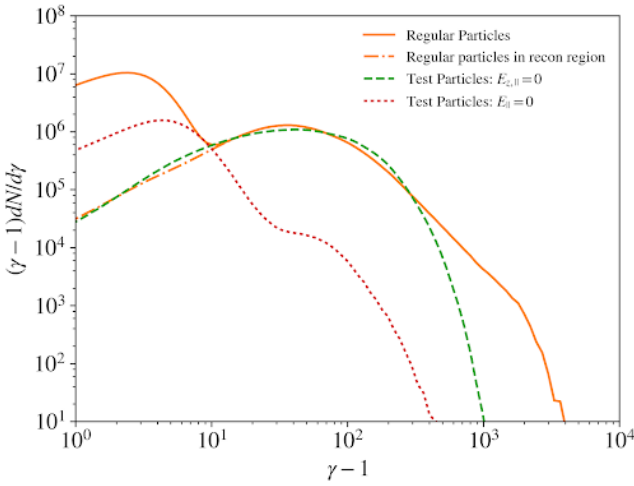


Figure 14. Spectra of different populations of particles. The regular particle spectrum is shown in orange, the solid line corresponds to the spectrum of particles throughout the entire simulation domain while the dash-dot line shows the spectrum from the reconnection region. The green dashed line shows the spectrum of test particles that do not experience parallel electric fields in the z-direction and the dotted red line shows the spectrum of particles that do not experience any parallel electric fields. The spectra for test particles are computed only in the reconnection region.

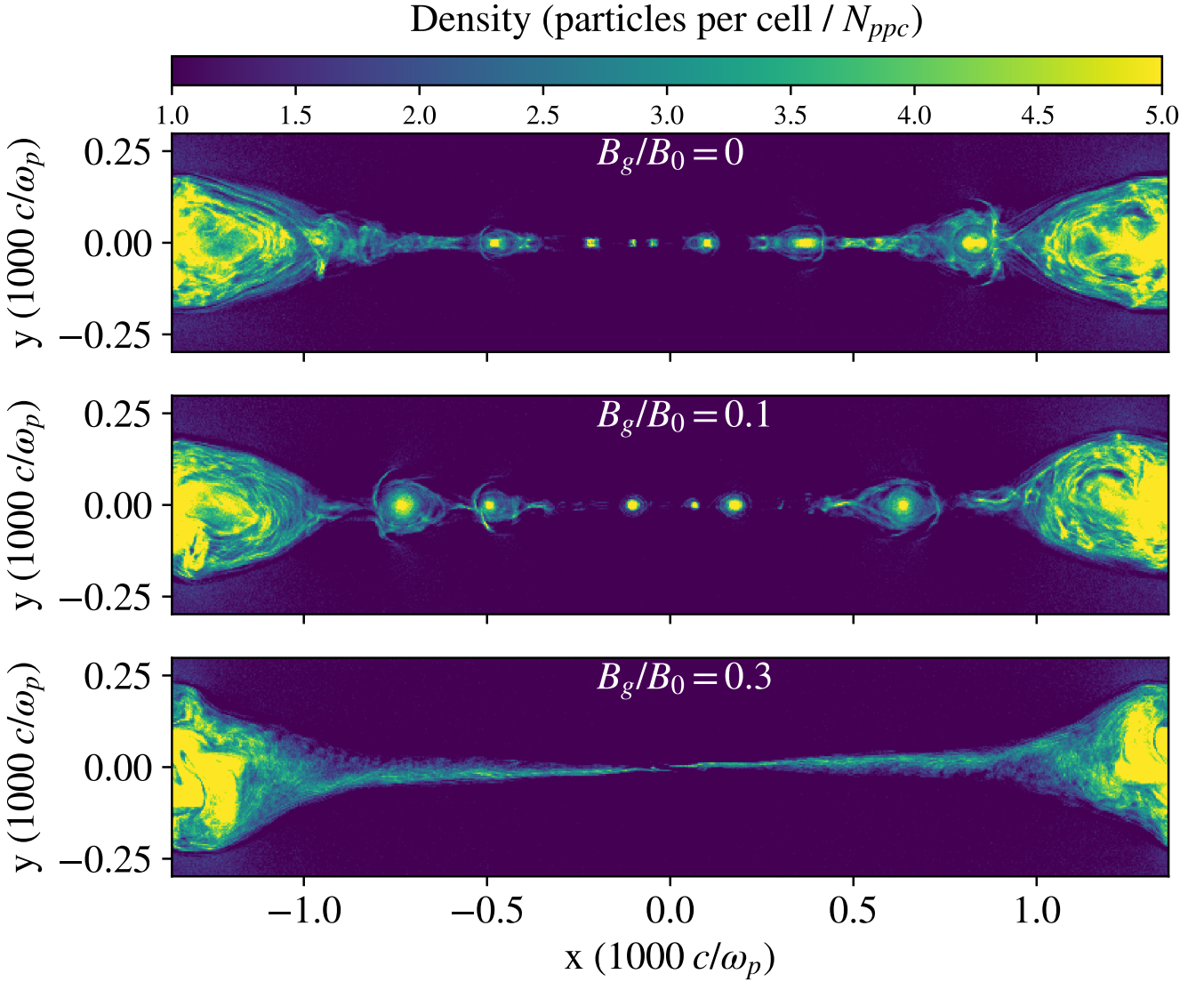


Figure 16. Snapshots of density for simulations with varying guide field. We see that the structures in the purely anti-parallel case (top) and the weak guide field ($B_g = 0.1$) cases are remarkably similar; plasmoid and x-point formation occur copiously via the secondary tearing mode throughout the reconnection layer. The higher guide field case (bottom) only shows a single x-point because the secondary tearing mode is suppressed.

REFERENCES

- Ball, D., Sironi, L., & Özel, F. 2018, ApJ, 862, 80
- Buneman, O. 1993, in “Computer Space Plasma Physics”, Terra Scientific, Tokyo, 67
- Dahlin, J. T., Drake, J. F., & Swisdak, M. 2014, Physics of Plasmas, 21, 092304
- Guo, F., Liu, Y.-H., Daughton, W., & Li, H. 2015, ApJ, 806, 167
- Haggerty, C. C., Parashar, T. N., Matthaeus, W. H., et al. 2017, Physics of Plasmas, 24, 102308
- Li, X., Guo, F., Li, H., & Li, G. 2017, ApJ, 843, 21
- Nalewajko, K., Uzdensky, D. A., Cerutti, B., Werner, G. R., & Begelman, M. C. 2015, ApJ, 815, 101
- Servidio, S., Matthaeus, W. H., Shay, M. A., Cassak, P. A., & Dmitruk, P. 2009, Phys. Rev. Lett., 102, 115003
- Spitkovsky, A. 2005, in AIP Conf. Ser., Vol. 801, Astrophysical Sources of High Energy Particles and Radiation, ed. T. Bulik, B. Rudak, & G. Madejski, 345
- Wang, H., Lu, Q., Huang, C., & Wang, S. 2016, ApJ, 821, 84
- Werner, G. R., & Uzdensky, D. A. 2017, ApJ, 843, L27